Can stochastic slip rupture modeling produce realistic **M**9+ events?

Small[1], David T. & Melgar[1], Diego

[1]University of Oregon

Corresponding email: dsmall2@uoregon.edu

Abstract:

Stochastic slip rupture modeling is a computationally efficient reduced-physics approximation that has the capability to create any number of unique ruptures based only on a few statistical assumptions. Its simplicity and efficiency make it an attractive and viable option for testing early warning systems, hazard assessments, and infrastructure response studies. Yet a fundamental question pertaining to this approach is whether the slip distributions calculated in this way are "realistic". More specifically, can stochastic modeling reproduce slip distributions that match what is seen in **M**9+ events recorded in instrumental time? Here, we start with the 2011 **M**9.1 Tohoku-oki earthquake and tsunami where we test both a stochastic method with a homogeneous background mean model and a method where slip is informed by an additional interseismic coupling constraint. We test two coupling constraints with varying assumptions of either trench-locking or -creeping and assess their influence on the calculated ruptures. We quantify the dissimilarity of slip distribution between the 12,000 modeled ruptures and a slip inversion for the Tohoku earthquake. We also model tsunami inundation for over 300 ruptures and compare the results to an inundation survey along the eastern coastline of Japan. We conclude that stochastic slip modeling can produce ruptures that can be considered "Tohoku-like", and inclusion of coupling can both positively and negatively influence the ability to create realistic ruptures. We then expand our study and show that for the 1960 **M**9.4-9.6 Chile and 2004 **M**9.1-9.3 Sumatra events, stochastic slip modeling has the capability to produce realistic ruptures.

Plain Language Summary:

Stochastic slip rupture modeling is an effective and simple method for generating a unique number of earthquakes based on only a few statistical parameters. Although the parameters that define these synthetic ruptures are calculated from real earthquakes, the determined slip patterns from this approach have not been tested to see whether they are "realistic" or not. Here, we answer the question of can stochastic modeling reproduce slip distributions that match what is seen in **M**9+ events recorded in instrumental time? We start with the 2011 **M**9.1 Tohoku-oki earthquake and tsunami where we test both a more traditional approach to stochastic modeling as well as an approach that utilizes a fault zone's pattern of geodetic coupling to inform slip. We quantify the dissimilarity of slip distribution between the ruptures and a Tohoku earthquake model. We also generate tsunami models for some ruptures and compare their results to an inundation survey following the Tohoku earthquake. We conclude that stochastic slip modeling can produce ruptures that can be considered "Tohoku-

like". We then expand our study to and show that for the 1960 **M**9.4-9.6 Chile and 2004 **M**9.1-9.3 Sumatra events, stochastic slip modeling has the capability to produce realistic ruptures.

Key Points:

- Stochastic modeling can reproduce **M**9 ruptures with low dissimilarity.
- Based on the combined analysis of the Tohoku event and tsunami, we conclude a rupture must be under a dissimilarity of 20 to be realistic.
- Including coupling into the stochastic method can have a positive or negative influence based on the "correctness" of the input coupling model.

1. Introduction:

Unlike other rupture modeling techniques, stochastic slip modeling utilizes a reduced-physics approximation. Rather than solving for a fully dynamic rupture that includes physics-based fault zone characteristics like stress drop, fault zone material properties, and friction, stochastic modeling assumes that ruptures can be more simply described by only a few different statistical parameters inferred from observations of real earthquakes (Mai & Beroza, 2002). In this view, slip distributions are realizations of an underlying probability density function. With this assumption, the computational cost of determining ruptures for large magnitude events is reduced significantly, allowing for a greater quantity of unique ruptures to be calculated in a short amount of time. Studies that have shown to greatly benefit from use of stochastic hypothetical models include earthquake early warning where ruptures produced can be used to train advanced machine learning algorithms (e.g., Lin et al., 2021), as well as to seismic and tsunami hazard assessments where ruptures inform localized hazards (e.g., Graves et al., 2011; LeVeque et al., 2016; Small & Melgar, 2021).

As new earthquakes occur, there have been numerous efforts to validate the different scaling laws and statistical parameters underpinning the stochastic approach (e.g., Goda et al., 2016; Melgar & Hayes, 2019). However, whether these synthetic ruptures have the potential to mimic real very large magnitude earthquakes (M9+) for a given area has not been explored. There have been proposals to incorporate more detailed geophysical knowledge while maintaining computational efficiency into stochastic slip models. Small and Melgar (2021) proposed a way to utilize fault interseismic coupling to inform slip distribution in the stochastic workflow. In this method, the goal is to use a fault zone's coupling pattern to inform stochastic slip distributions so that the resultant hypothetical ruptures can be more representative of the specific region's earthquake potential. Interseismic coupling is related to the ratio between the motion on a fault during the interseismic period and the relative plate velocity (Metois et al., 2016). For many large recent large ruptures where coupling models existed prior to the

event, a relative correlation between large coseismic slip patches and regions of high coupling ratio has been noted. This correlation is seen at subduction zones globally including Chile (Metois et al., 2013; Barnhart et al., 2016), Peru (Perfettini et al., 2010; Villegas-Lanza et al., 2016), Alaska (Li & Freymueller, 2018), and Japan (Loveless & Meade, 2015). By including coupling in the modeling process, ruptures may have a greater potential of being more realistic to the given area of interest. Yet this correlation does not equate to causation. For instance, some previous earthquakes have ruptured only a portion of the highly coupled zone (e.g., Konca et al., 2008; Moreno et al., 2010) or with large slip patches within more intermediate coupling zones like the 2007 **M**8.0 Pisco earthquake (Perfettini et al., 2010). Similarly, our lack of instrumentation offshore in the shallow most portion of the subduction zones creates great uncertainty and poor resolution for determined coupling models (e.g., Wang & Trehu, 2016; Lindsey et al., 2021). So, the question of the validity of the ruptures produced is once again important to answer.

Here, we explore this problem specifically. Can stochastic slip rupture modeling reproduce slip distributions that match great earthquakes recorded in instrumental time? Also, if interseismic coupling is included as an a priori constraint on the stochastic approach, does this better reproduce large ruptures? We use this study as a formal check for the application of stochastic slip modeling in calculating realistic large ruptures. If we can reproduce slip distributions of those calculated for real, large ruptures, we can add confidence to the value and implementation of stochastic modeling for past and future work.

To answer these questions, we look at three different **M**9+ events: **M**9 2011 Tohoku-Oki, **M**9.1-9.3 2004 Sumatra, and **M**9.2-9.4 1960 Chile. Since reliable coupling models are not available for all three of the proposed events, we only compare the influence of the coupling constraint for the 2011 Tohoku-Oki event. We compare modeled slip distributions to previously published finite fault slip inversions for each of the three ruptures. The assessment of slip distributions is done using a metric to determine the dissimilarity between the patterns. We first focus on the 2011 Tohoku-Oki event and compare three different rupture classes to the slip model from Minson et al. (2014). Two of these rupture classes utilize the coupling constrained stochastic approach, each constrained by different end member coupling models from Loveless and Meade (2016). The other class of ruptures uses a homogeneous slip potential for the stochastic approach, which can be considered the more traditional approach (e.g., Frankel et al., 2018). We obtain unique dissimilarity values for each class. For a subset of these ruptures, we model tsunami inundation for the eastern coast of Japan between 35°-41°N and compare the inundation results to a survey proceeding the 2011 tsunami by Mori et al. (2012). In combination with the dissimilarity metric and the inundation data, we obtain a threshold for the dissimilarity metric for which we can consider a rupture "Tohoku-like", or for judging other ruptures, "realistic". We analyze the influence of coupling on the ability of stochastic modeling to reproduce large ruptures in comparison to the traditional stochastic modeling. With this dissimilarity threshold for realistic ruptures, we widen our focus on

two other subduction zones and determine whether stochastic modeling has similar capabilities irrespective of rupture or region. In short, we find that stochastic slip rupture modeling can reproduce slip distributions for all three **M**9+ ruptures presented reasonably well. For the 2011 Tohoku-Oki earthquake, including the coupling constraint, has varying effects on the results: one coupling model noticeably improved the similarity to the Tohoku earthquake, and one was not able to produce any ruptures that were similar to the earthquake.

2. Data and Methods:

2.1 Input models:

We focus on the 2011 **M**9 Tohoku-Oki first since it is the best studied great earthquake (Lay et al., 2018). The ruptures calculated using the coupling constraint technique, along with ones generated without the constraint, will be compared to a slip distribution model for the 2011 Tohoku-Oki **M**9 rupture. The Honshu Island region of Japan is the most densely instrumented areas globally for geophysics-based observations. The dense instrumentation and the great societal impact of the rupture made this heavily focused in the scientific community, where tens of slip inversions were determined for the rupture (e.g., Ammon et al., 2011; Yue and Lay, 2011; Satake et al., 2013; Minson et al., 2014). We focus on only one of the models for the earthquake from Minson et al. (2014) (hereafter called the "Minson model"), expressed in Figure 1a. The Minson model is a fully Bayesian inversion, determined from simultaneously inverting for 1Hz kinematic GPS data, static GPS offsets, seafloor geodesy, and tsunami data. This model concentrates most of the slip of the rupture between 10-20km in depth, with the magnitude of slip reaching almost 80m high within this region. More information about the slip model can be found in Minson et al. (2014).

A fault's geodetic coupling is defined by the ratio of the slip deficit and the local plate convergence rate. 100% coupling thus means the fault is kinematically locked and accumulating a slip deficit at the rate of plate convergence. 0% means that it is creeping at the rate of plate convergence. Rather than coupling, throughout the article we implement the slip deficit rate (SDR) as prior information for rupture generation. We focus on the SDR and apply these models to our stochastic methodology, as expressed in the proceeding section 2.2.

We look at two different SDR models for the Japan trench from Loveless and Meade (2016) (Figure 1b and 1c). Both models are constrained using roughly 19 years (1996-2014) of geodetic observations from the GEONET network. The time-series data is then split into five, 3.75-year epochs and the SDR models are determined using a block model approach (Meade and Loveless, 2009). The final SDR models are calculated by taking the average of the results of the five epochs. The models are determined using the same inputs as one another; however, they vary based on an imposed constraint of coupling at the trench. Figure 1b imposes a constraint that the shallowest portion of the subduction zone creeps at an equal rate as the Pacific Plate rate. This model follows the idea that the shallowest portion of the megathrust cannot accumulate interseismic elastic

strain. This is thought to be the result of the high percentage of clay composition at the trench (Oleskevich et al., 1999). On the other hand, Figure 1c eases this constraint, permitting variable coupling to occur up to the trench. Due to the lack of instrumentation offshore, the shallowest portions of the megathrust are poorly resolved, evident by the wide variability in SDR between the two models. Without more robust offshore GNSS instrumentation, determining which model is more accurate is nearly impossible. Therefore, we utilize both models for the study.

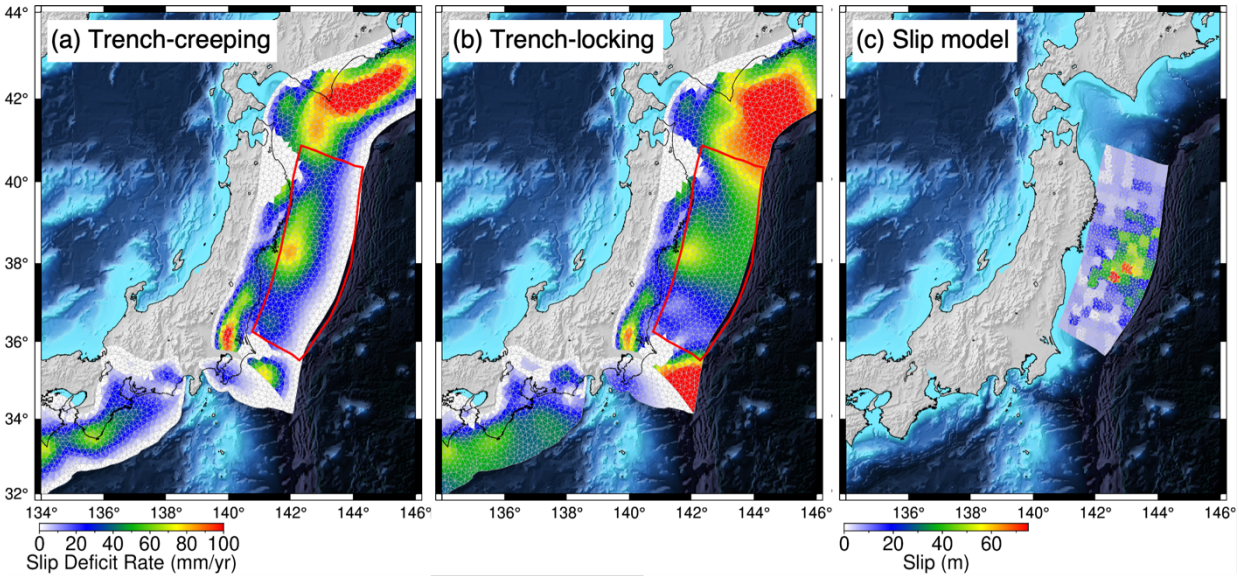

Figure 1: (a) Finite fault slip inversion from Minson et al. (2014). Maximum slip over 75m. All models show the final rupture domain for the stochastic modeling. (b) "Trench-creeping" SDR model with the imposed constraint of creeping (or SDR = 0mm/yr) from 5km downdip to the trench. (c) "Trench-locking" slip deficit rate (SDR) model where no constraint on coupling near the trench so slip deficit is present up to the trench. Both coupling models come from Loveless and Meade (2016).

2.2 Stochastic modeling:

Here, we briefly detail the method of stochastic modeling, as well as how coupling patterns are introduced in the process to inform the resultant slip patterns. These methods can be found described in greater detail in LeVeque et al. (2016), Melgar et al., (2016) and Small & Melgar (2021).

The first step is to define the megathrust as a 3D mesh surface composed of discrete subfaults using the three-dimensional finite element mesh generator, GMSH (Geuzaine and Remacle, 2009). The slab mesh is generated from the Slab2 model from Hayes et al. (2018) with an average subfault length of 15km. Once the mesh is defined, a subfault is selected at random as the synthetic

rupture hypocenter. For a given target magnitude, the rupture length and width are determined based on a probabilistic scaling law (Blaser et al., 2010), where the dimensions of slip are magnitude dependent based on a log-normal distribution of slip. As the rupture magnitude increases, the dimensions of the rupture also on average increases. The log-normal distribution allows for variability within the dimensions of ruptures of equal magnitude.

Then, we utilize the method of stochastic modeling introduced by Mai and Beroza (2002) to calculate the rupture itself. Using the von Karman autocorrelation function (VK ACF) to model slip as a spatially random field and defining correlation lengths along-strike and -dip, the stochastic rupture is defined. In this approach, there are only three necessary assumptions needed to define earthquake slip patterns: the correlation lengths in the along-strike and down-dip that define the dominant asperity size of the rupture, and the Hurst exponent that models the roughness of the slip pattern. We use the results from Melgar and Hayes (2019) for defining correlation lengths based on a log-linear scaling of magnitude and correlation lengths and a magnitude independent Hurst exponent. The stochastic method above is expressed in the spectral domain of slip rather than spatial. To account for 3D fault geometries and enforce prior constraints (e.g., geodetic coupling), we apply the Karhunen-Loeve (K-L) expansion to the VK-ACF, where slip is now represented in the spatial domain (LeVeque et al., 2016). The K-L expansion states that a slip vector, s, is described as

$$s = \mu + \Sigma_{k=1}^{N} z_k \sqrt{\lambda_k \nu_k}. \quad (1)$$

This defines s as the sum of the mean slip, μ, and the summation over the desired number of eigenmodes, N, of the eigenvalues and eigenvectors from the VK-ACF, λ_{k} and ν_{k}. Further stochastic behavior of the resultant ruptures is included in the equation as $\mathrm{z_k}$, which are normally distributed random numbers with a mean of 0 and a standard deviation of 1. The variable z allows us to create any number of unique slip distributions for a given magnitude and rupture dimensions. For ruptures where all subfaults have equal potential for slip and no prior constraints are applied, μ is simply a homogeneous mean model with enough slip to match the desired target magnitude. However, we can instead impose a mean slip model that is informed by the coupling pattern as μ. For instance, for a given desired magnitude and rupture dimensions are selected from the scaling laws, the coupling pattern is re-scaled for the segment into slip pattern. This is then used as μ and stochastic variability is applied to create the output ruptures. Once again, more information on the stochastic process is detailed in Small & Melgar (2021).

It is important to note here that in the coupling constrained methodology, the coupling models do not inform how much slip will occur at a given location. But rather, it provides a greater probability for areas of high SDR to have greater coseismic slip. It is still possible in this method for a region of high SDR to rupture in smaller slip than a region with relatively smaller SDR. In this method however, regions where SDR = 0 will never be able to produce coseismic slip. The actual influence of the coupling constraint is often difficult to discern for a

single given rupture, but in observation with a large suite of ruptures, the mean pattern of slip for all the ruptures in the suite resembles the initial coupling pattern constraint.

To calculate the ruptures, we use the Fakequakes module of the open-source forward modeling and inversion code MudPy (Melgar & Bock, 2015; Melgar, LeVeque, et al., 2016; Melgar, 2020; Small & Melgar, 2021) that can calculate both homogeneous and coupling constrained rupture models. For each of the three classes mentioned prior, we calculated a total of 4,000 ruptures with a starting magnitude between **M**8.8 and **M**9.2 in magnitude bins of 0.1. Maximum slip on any given subfault is limited to 100m. Although this is quite large, the 2011 Tohoku-Oki event is considered to have slipped over 70m in some patches (Minson et al., 2014). Our modeled domain for the ruptures follows slip distribution from the Minson model (Figure 1a). The rupture domain lies between 35°N and 41°N, with a down dip limit of slip at 50km depth. Rupture area and magnitude are unconstrained, so any portion of the domain may be considered or neglected, and the final magnitude for a given area may vary from the starting magnitude based on dimensions and scaling laws. Example ruptures are imaged in Figure 3 and 4. Similar Fakequakes setup for homogeneous mean model ruptures is implemented for the Sumatra and Chile earthquakes. More information on the setup is described in section 3.3.

2.3 Dissimilarity metric:

Since we are interested in comparing the generated stochastic slip distributions to known slip inversions, it is important to define a quantitative assessment of likeness between models. To assess this quantitatively and objectively, we calculate the numerical dissimilarity between ruptures using the normalized square metric (Kragh & Christie, 2002; Razafindrakoto et al., 2015). There are other metrics for quantifying dissimilarity (e.g., grey scale metric, Wilson et al., 1997), however, we focus on the normalized square metric as it is both numerically simple and efficient. Because we are focused on determining the ability of stochastic slip rupture modeling to reproduce realistic large ruptures, working directly with slip pattern dissimilarity is ideal.

In comparison to other dissimilarity metrics, the normalized square metric is best for capturing the magnitude differences between two objects and is sensitive to image translation. The normalized square mean metric expresses dissimilarity, D, as

$$d(A,B) = 100\frac{\Sigma_i[A(i)-B(i)]^2}{(\Sigma_i[A(i)]^2+\Sigma_i[B(i)]^2)/2} \ . \quad (2)$$

Dissimilarity between two slip models, A and B, is expressed as the square of the difference between the models divided by the mean of the individual squared values. A and B in the equation are regular grids. Prior to interpolating to a regular grid, we first interpolated the Minson model to the Slab2 geometry to maintain uniformity in the process. We then interpolate the 3D triangular mesh ruptures and slip model using the spline interpolation method.

Kragh and Christie (2002) previously define this metric as a percentage with values between 0 and 200%. For ease of understanding, we scale the dissimilarity metric by dividing it by two, making it a metric from 0 to 100. The more dissimilar the two models are from one another, the greater the value. D = 0 denotes identical slip models and the greater the differences between the two models, the greater the value of d is.

2.4 Tsunami inundation modeling

Although the dissimilarity value provides a basis for quantifying likeness between the slip models, the values themselves do not provide a clear threshold that we can use to denote whether a rupture is "Tohoku-like". Further, slip inversions are inherently uncertain so while low dissimilarity between model and inversion is encouraging, it is somewhat limited in being a satisfactory assessment that the rupture indeed replicates reality. To determine the dissimilarity value threshold for what can be considered a "Tohoku-like" rupture, we model tsunami inundation and compare inundation values to recorded survey points. This analysis provides an observable phenomenological rationale for comparing impacts of ruptures.

Post-event tsunami inundation surveys measure the maximum height of the tsunami wave propagation onshore. Here, we define inundation with respect to mean sea level. We model inundation at 3,244 survey points from Mori et al. (2012) (Figure 2). In the inundation study, they record over 5,000 total tsunami data points onshore between 35°- 41°N. In their dataset, they also record run-up height, which is the maximum height the tsunami propagated to onshore (the run-up distance) with respect to sea level. We do not consider these points for our study since modeling for run-up distance and height is difficult to do. The dataset for inundation is extensive along the coast, however, a gap in data between roughly 37°-38°N is present. Data distribution is not recorded equally in latitude, with the greatest abundance of points in the Sendai Bay and Sanriku Coast in Iwate Prefecture (37.5°-38.4°N). Maximum recorded coastal inundation values reached up to 40m high.

To model tsunami inundation for calculated ruptures, we first must determine the resultant coseismic vertical deformation to be applied as the initial condition for tsunami wave generation. We utilize the analytical solution for angular dislocation for triangular subfaults in an elastic half space (Comninou & Dunders, 1975), which is an adaptation of the Okada equations for rectangular subfaults (Okada, 1985). Models are calculated using the finite volume, 2D depth-average, non-linear tsunami modeling code Geoclaw (http://www.clawpack.org/geoclaw) (LeVeque, George, et al., 2011). We assume instantaneous rupture generation since rupture propagation velocities are much faster than tsunami wave velocities (Williamson et al., 2019).

We model tsunami generation and inundation for points between 34.5°-41°N. Since we are interested in wave propagation on land, topography and shallow water bathymetry must be sampled with very fine resolution. Because our mod-

eled domain is quite extensive (7° in latitude and longitude) and we need fine resolution bathymetry and topography data for coastal regions, we utilize one coarser bathymetry/topography file for the entire domain and finer scale subregions for the coastal areas of interest to decrease computational cost. We use SRTM15 with a sampling rate of 15 arcseconds (~450 m pixels) for our overall bathymetry/topography domain (Tozer et al., 2019). We then stitch together SRTM1 topographic data (1 arcsecond sampling rate, ~30 m pixels) and 1 arcsecond bathymetry data from the "M7000" data set purchased from the Japan Hydrographic Association in 8 rectangular segments that extend to 200m below sea level between 34.5°N and 41°N. We resample these fine segments from 1 to 3 arcseconds as 1 arcsecond was too costly for the tsunami models to run even with 40 CPUs in hand. To increase efficiency even more, we utilize the adaptive mesh refinement (AMR) within GeoClaw so as the more complex portions of tsunami propagation occur and proximity to regions of interest decrease, the mesh can adaptively become finer. We use 5 different AMR levels that go from coarsest to finest: 1', 30", 15", and 3", respectively.

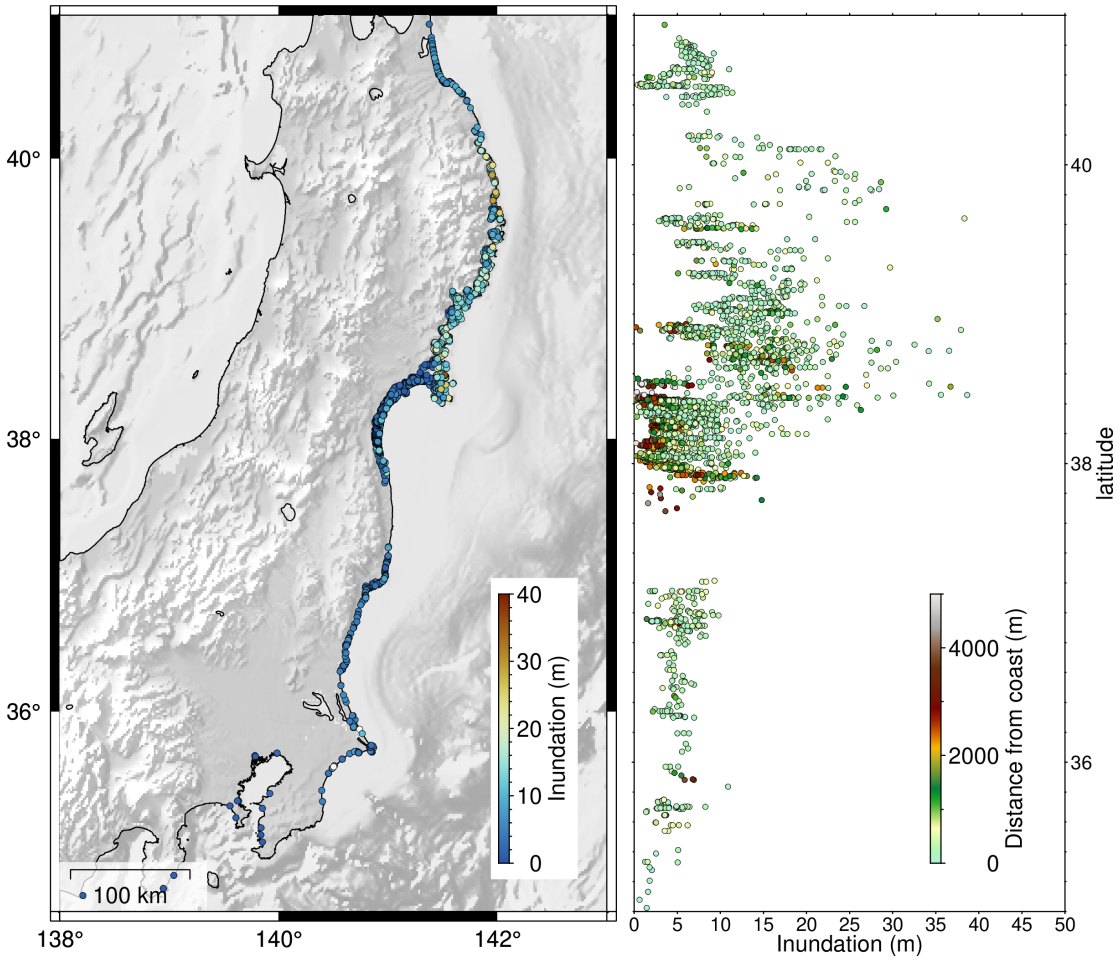

Figure 2: *Tsunami inundation survey of the 2011 Tohoku-oki tsunami from Mori et al. (2012). (a) Map view*

Even with these capabilities to increase efficiency, running inundation for over 3,000 points along a region of 7° latitude is costly. Running on 25 threads, tsunami inundation models took over 4 hours for each to complete. Rather than running 12,000 tsunami models for the combined three classes, we instead took a subset of ruptures, totaling 330. These ruptures were chosen at random, however, we biased adding more ruptures with lower dissimilarities (below D = 50).

3. Results:

3.1 Rupture Modeling and Dissimilarity:

In total, 12,000 ruptures were generated for the three different rupture classes. Although initial magnitudes ranged from **M**8.8-9.1, final magnitudes fall between **M**8.6-9.4 since we modeled ruptures without magnitude constraint. There

is no clear distinction in the final magnitude range between any of the rupture classes. Rupture dimensions varied, however, due to the confined model domain to the Minson model, there was a bias of ruptures to slip the entire domain.

For all ruptures, we calculate the dissimilarity between the slip distribution and the Minson model using the normalized squared metric. The values for all ruptures are shown in Figure 3a-c, where they are plotted in histograms based on rupture class. From the histograms, we can split the three classes into two distinct groups based on their sense of distribution. The trench-creeping class produces no ruptures below a metric of 35. The distribution has a maximum around a dissimilarity value of 60. The trench-locking and homogeneous classes, on the other hand, have a dissimilarity distribution relatively like one another. The minimum dissimilarity for the two classes is 12 for the trench-locking and 16 for the homogeneous class. To first order, the two classes appear to have similar rupture dissimilarity distributions, yet there is a bias in the trench-locking ruptures towards lower values of dissimilarities overall. In comparison to the trench-creeping class, the homogeneous class has almost 400 ruptures below the least dissimilar trench-creeping rupture, about 10% of the total homogeneous ruptures. The trench-locking class, however, has almost 600 ruptures below the trench-creeping class, or 15%.

From these dissimilarity values, we would like to determine a cutoff value for ruptures to be considered "Tohoku-like". The accompanying rupture models in Figure 3 show three ruptures for each class with varying rupture dissimilarities. We generally see noticeable differences between ruptures with the lowest dissimilarities (Figure 3 d, g, and j) and the highest dissimilarity (Figure 3 f, i, and l). Besides the lowest dissimilarity ruptures, it is difficult to confidently distinguish just by observation which rupture has the lower dissimilarity in the second two columns. There is a trend for ruptures below a metric of 35 to have large slip patches around 38°N and between 10-30km downdip similar to the Minson model. Because the normalized square metric assesses dissimilarity by a point-by-point comparison, even if a rupture has a similar asperity size and shape to the Minson model, if the location of the patch is offset, this will influence the dissimilarity outcome. This metric is also more heavily affected by larger slip differences. So, if larger slip patches are not represented or represented in other areas than the location of the Tohoku large slip patch, this negatively influences the outcome dissimilarity. As the rupture dissimilarities increase, the variability in the patterns of slip distribution increases. For instance, some ruptures with larger dissimilarities do not rupture up-dip and some experience their largest slip patches farther North or South of the Tohoku slip patch in disagreement to the Tohoku earthquake. Recall our goal is to determine whether stochastic modeling can produce "realistic" ruptures. So, we next determine a dissimilarity threshold that both minimizes variability in synthetic ruptures and contains the dominant slip distribution of the Tohoku earthquake.

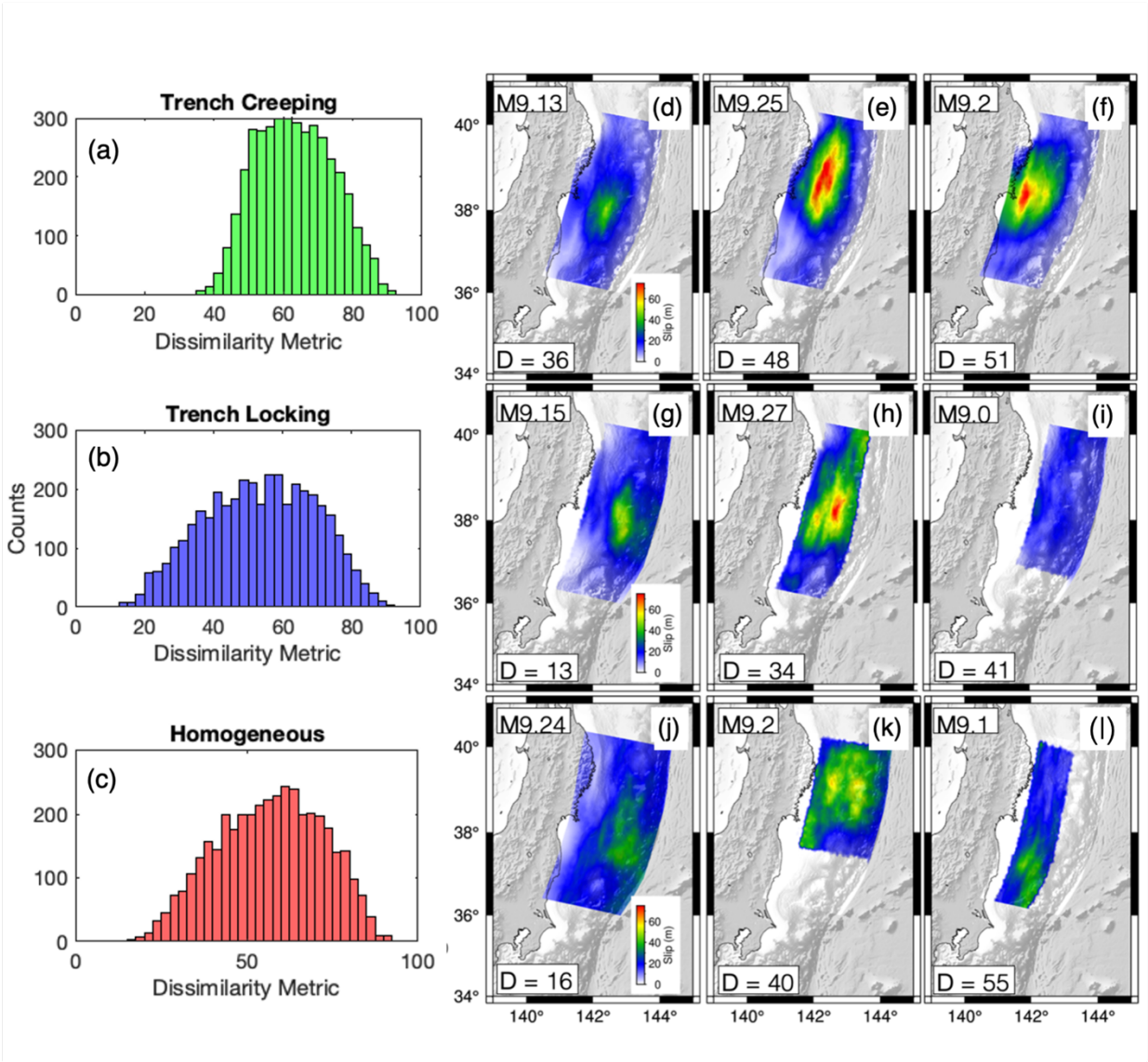

Figure 3: (a-c) Dissimilarity metric histograms with a bin width of 2.5 for the three rupture classes. (d-f) Exa

3.2 Tsunami Inundation Results:

By modeling tsunami inundations, we can quantify the physical effects of differences in the dissimilarity values. For each of the 330 ruptures we model tsunami propagation and inundation at 3,244 survey points from Mori et al. (2012). We compare the inundation residual between the modeled points and the surveyed points using the root mean squared error (RMSE), and we also look at the percentage of points inundated, regardless of inundation height. It

is worthwhile to note here that for all 330 ruptures, the RMSE of inundation has a minimum just below 7m and a maximum just over 10m. There is not a wide array of RMS values. For all ruptures, the Sanriku coast (between 38°N and 39°N) has the largest discrepancies between the model and survey. This region also experienced the largest coastal inundation following the 2011 earthquake, with some areas reaching almost 40 meters in amplitude. Inundation residuals between modeled points and surveyed points have the largest values in the Sanriku coastal region, likely due to the wider recordings of inundation values. If we look at residuals based on distance from the coast, we observe on average the further the inundation point was recorded, the smaller the residual is (Figure 4c).

Figure 4 shows two example ruptures with differing dissimilarity values and their tsunami inundation models. The first example is a rupture of dissimilarity value of around 12. In comparison to the post-event survey, the model inundated 92% of the 3,244 survey points. The RMSE of the inundation model is just above 7m in relation to the survey. The modeled tsunami residuals for this rupture are biased towards the positive which represents a larger tsunami than the recorded tsunami. This suggests that considering both a very low dissimilarity value and a high percentage of points inundated is a useful heuristic tool for determining whether a rupture is "Tohoku-like". In contrast, the second rupture shown has a dissimilarity much greater than the first, with D =50.65. From inspection of the slip distribution, we can see that it does not contain a large shallow slip patch as required by the Minson slip inversion. This rupture rather experiences the largest slip towards the North of the domain. Its tsunami model only inundates 56% of the survey points, far less than the 92% inundation from the previous rupture. This rupture does not appear to inundate far inland from the coast - almost all survey points past 1km do not experience inundation. We can see from this example that this rupture should not be considered "Tohoku-like" since it has such a high dissimilarity and fits the inundation data poorly.

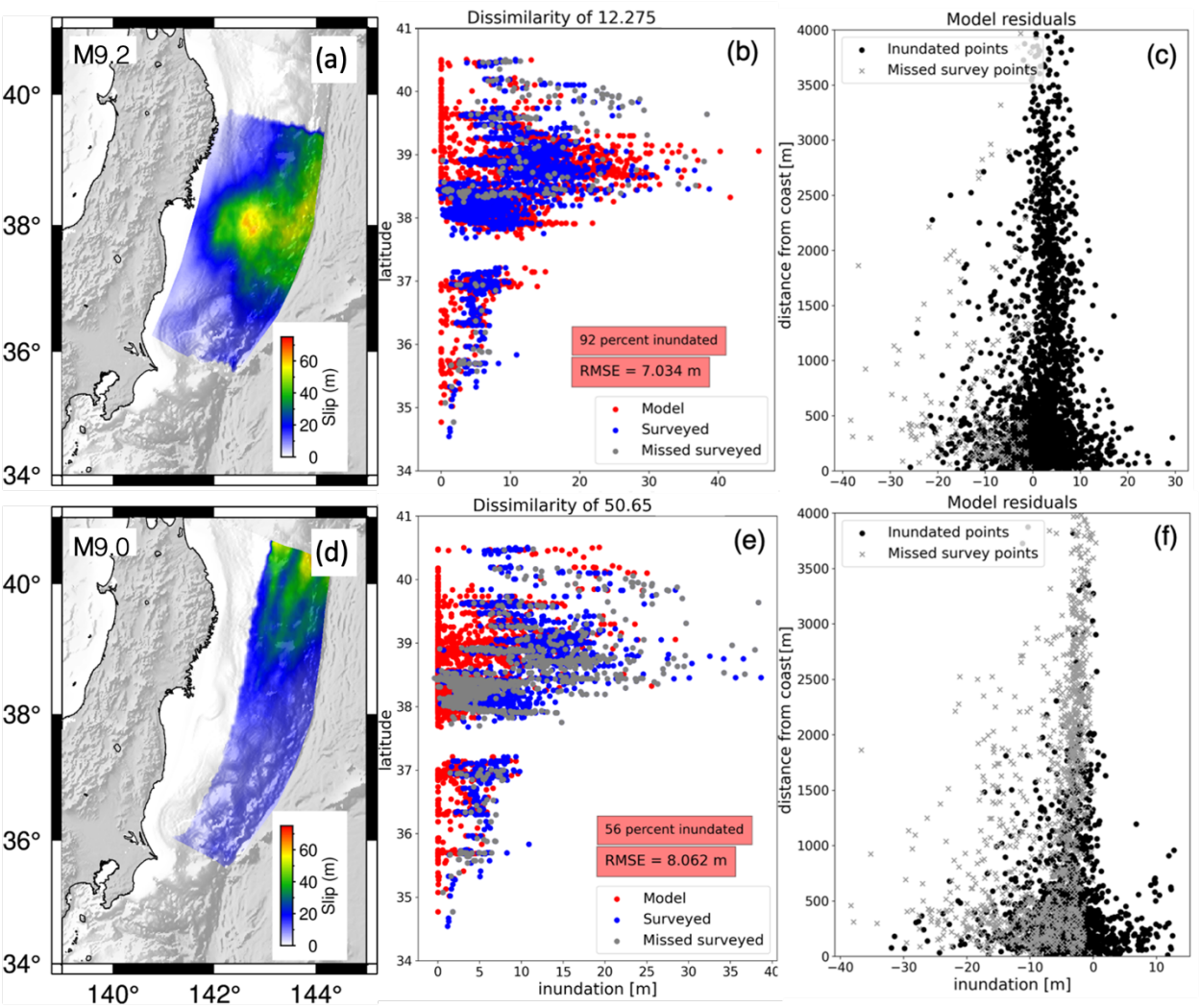

*Figure 4: (a) **M**9.2 rupture model in the trench-locking class. (b) Inundation in meters at each of the survey*

If we consider all the ruptures that we performed inundation modeling for, we can obtain a better sense of the relative importance and threshold for the dissimilarity metric. In Figure 5, the dissimilarity metric is plotted with respect to the inundation percentage for all three of the rupture classes. Each scatter point is scaled by the rupture's RMSE for inundation. There is a clear distinction between ruptures with high and low dissimilarity values. The points generally follow a linear path along which the dissimilarity metric decreases, the inundation percentage increases and the RMSE decreases. So, as the ruptures approach the top left corner of the plot, the ruptures become more "Tohoku-like". There is some variability associated with these metrics, especially in the more moderate (30-60) dissimilarity values. For instance, for a given dissimilarity value, inunda-

tion percentage varies almost 40-50%; however, as the dissimilarity percentage decreases, the degree of variability in all metrics decreases.

To determine a threshold for what we can consider to be a "Tohoku-like" rupture, we look for dissimilarity values that both maximize the inundation percentage and minimize the RMSE. From the results, we fit the threshold for what can be considered a "Tohoku-like" rupture is a dissimilarity of 20. At this threshold, inundation percentage for all points is over 80%, where there is also the smallest variation in the distribution of inundation percentages. The RMSE for all ruptures is consistently under 8m, with an average RMSE of 7.34m, which is over 1m smaller than the total average. There are 57 trench-locking, 14 homogeneous and 0 trench-creeping ruptures that fit this threshold. If we increase the threshold by 5, we observe 169 trench-locking 68 homogeneous, and still no trench-creeping ruptures. Although an increase in the threshold of 5 still has a dominance of ruptures with over 80% inundation and RMSE average of 7.6m, the range in inundation results begins to widen much greater here (Figure 5). There is a general consistency in ruptures below a dissimilarity of 20, however, past 20 a sharper negative trend is present in inundation as the dissimilarity increases.

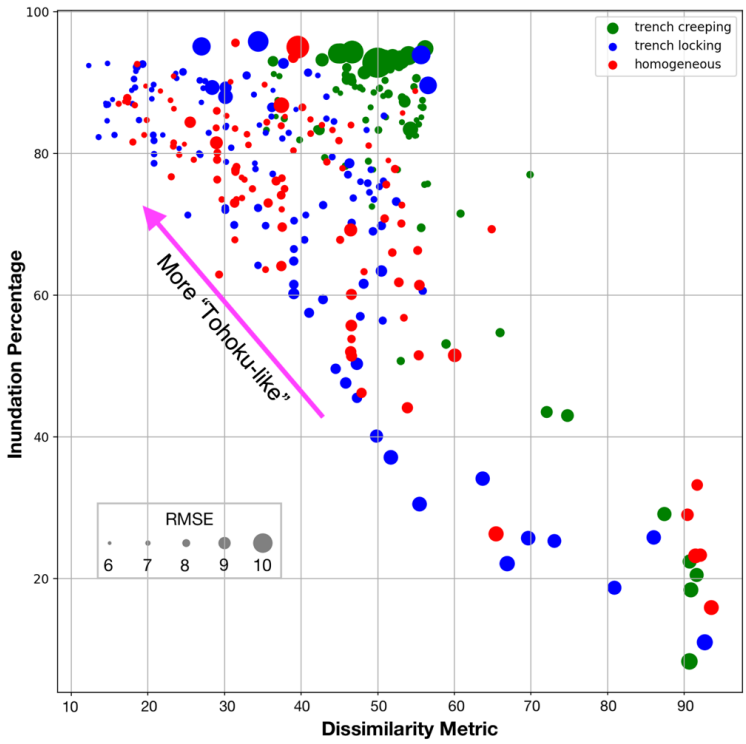

Figure 5: Dissimilarity metric versus inundation percentage plot for all 330 ruptures that we performed inund

There are some ruptures with almost 100% inundation that also have some of the largest RMS errors and variable dissimilarity. These ruptures occur in all the rupture classes, but there is an increased number of them in the trench-creeping class. These ruptures all have the common characteristic of imposing large slip patch at 30km downdip from the trench close to the shoreline of the Sanriku Coast. Although these ruptures experience their dominant slip deeper, the proximity to the coast and the extent of the maximum slip patches (over 60m on average) generate a large tsunami relatively close to the shore. It is important to recognize that although the tsunami inundation percentages are very high (over 95%), they have relatively larger dissimilarity values and very large RMSE. Even though one metric appeared similar, the combination of all the three metrics is important to determine the similarity to the real rupture.

It should also be noted that these metrics are not perfect indicators for determining if these ruptures are "Tohoku-like," or more broadly, "realistic". The distribution of inundation points from the survey are not equally distributed,

but rather are more densely concentrated along the Sanriku Coast and Sendai Bay. Here the largest conglomeration of points is present, which may in turn create a bias in the final RMSE. The tsunami data is used here to help understand the relative differences between dissimilarity values, however, it does not provide stand-alone weight to determine whether the ruptures are "Tohoku-like" or not.

3.3 Global ruptures

Now that we have determined that the stochastic modeling approach is able to replicate the slip distribution from the 2011 Tohoku-Oki event, we are now concerned with ascertaining whether this holds true for other large ruptures with varying slip distribution conditions at other subduction zones. Since we have already proposed a dissimilarity threshold for determining if a rupture can be considered realistic, we apply this threshold to stochastic models for comparing other events. The applicability of the threshold is important since ~**M**9 events with good inundation surveying and calculated slip inversions are not as readily available as they are for the 2011 Tohoku-Oki event. Instead, we utilize our predetermined threshold for other ruptures. Here, we will focus on two different ruptures: the 1960 **M**9.3-9.4 Chile and the 2004 **M**9.2 Sumatra ruptures. Since we do not have reliable coupling models for either event prior to the ruptures, we only model them using the homogeneous stochastic modeling approach.

3.3.1 1960 Chile

Following the same approach as the previous rupture, we utilize the finite fault slip inversion from Ho et al. (2019) ("Ho model", Figure 6b) and quantify dissimilarity between calculated ruptures and the Ho model. This model was determined by jointly inverting tsunami waveforms and local geodetic data obtained from post-even leveling surveys. The model indicates slip extending along-strike for over 800km and 150km along-dip. Slip is concentrated in three large slip asperities, each with a width of about 200-300 km. This event is unique for many reasons, but most famously for being the largest in instrumental history.

We model 2,500 ruptures in 0.1 magnitude bins between **M**9.2-9.6. The domain is constrained between 37-46°S along strike and a down dip limit of 50km. Ruptures are placed on the slab model from Rodriguez and Russo (2020) rather than the Slab2.0 model utilized prior since the latter only reaches to 45°S. The simple rectangular geometry of the Ho model is first interpolated to the same slab geometry as the modeled ruptures prior to dissimilarity analysis. We allow rupture dimensions to vary throughout the model domain, as well as allowing the final magnitude to be unconstrained. The rupture domain is subdivided into 1790 triangular subfaults, with lengths around 10km wide on average. Final magnitudes vary from **M**8.9-9.7.

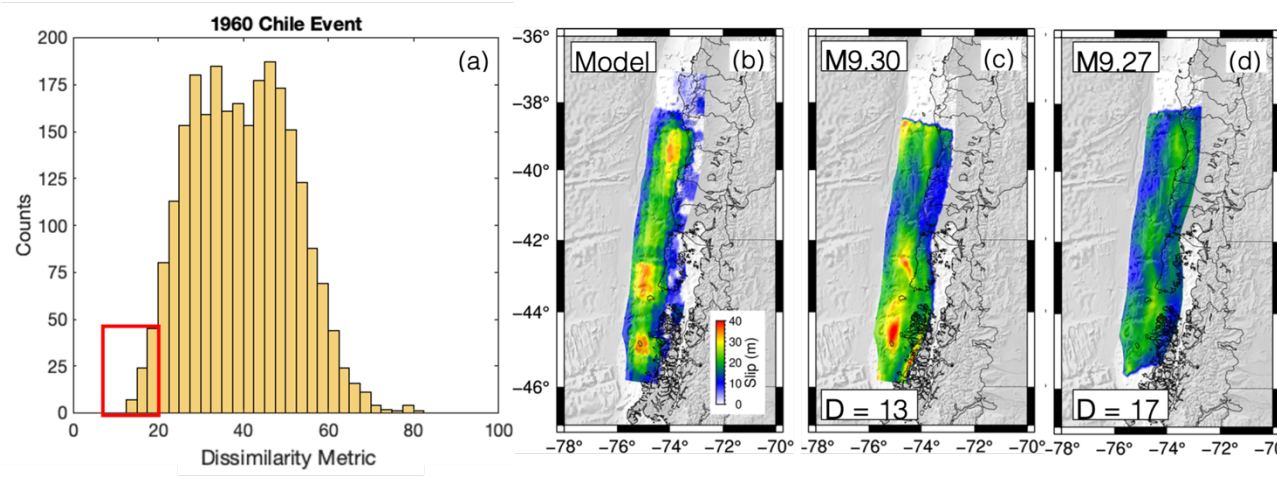

Figure 6: (a) Dissimilarity histogram distribution with a bin width of 2.5 for the 1960 Chile rupture. Red box

Using the same dissimilarity threshold that we previously determined, there are stochastic ruptures that can be considered realistic in relation to the Ho model. Figure 6c and 6d show two such ruptures. The first matches the maximum slip observed in the Ho model well and there appears to be three distinct slip patches that correlate well with the locations seen in the Ho model. This rupture has a dissimilarity of 13, which is the lowest in the suite of ruptures. The next rupture has a slightly higher dissimilarity of 17. Although the maximum slip observed does not reach over 30m as opposed to the 40m seen in the Ho model, the dominant slip patches are still relatively well resolved. There are 75 ruptures of the 2,500 total ruptures that fit the threshold. This is an increase in the percentage of ruptures that fall beneath the dissimilarity threshold in comparison to the homogeneous class for the Tohoku event (75 compared to 14 ruptures). There are almost 10 times greater ruptures that fit the Chile ruptures than there are for the Tohoku event.

3.3.1 2004 Sumatra

To model the 2004 Sumatra event, we use as a point of comparison the slip inversion from Rhie et al. (2007) ("Rhie model") that is the result of jointly inverting long period teleseismic data and local geodetic surface displacements (Figure 7b). This model is subdivided into 6 along-strike segments. One large slip asperity is in the southern portion of the rupture zone; however, slip extends almost 1300km along the Nicobar-Andaman Island chain. Although the large slip asperity reaches almost 40m, the relative size of the asperity is quite small in relation to the rupture region. This is not only one of the largest recorded ruptures, but also the spatially largest rupture in instrumental history.

Following from the previous analysis, we model 2,500 ruptures in 0.1 magnitude bins between **M**9.0-9.4. Since we do not fix final magnitude, final ruptures are between **M**8.8-9.6. We create a triangular subfault mesh from Slab2.0 (Hayes et

al., 2018) once more to model ruptures on. The model domain extends from 2°N to 14°N and slip is limited to above 50km down dip, with a total of 1084 subfaults of around 20-25km in length each. The Rhie model is first interpolated to the domain geometry and then both ruptures and the Rhie model are interpolated to a regular grid for the dissimilarity analysis.

Figure 7 shows two examples of rupture models that are considered realistic. The first rupture (Figure 7c) has a large slip patch of similar magnitude as the Rhie model and dispersed smaller slip (10m and below) throughout the rest of the model. The second rupture shown has a slightly larger dissimilarity value. The rupture is smaller than the Rhie model. Its dominant slip patch is located further south but close to the Rhie model and has more dispersed larger slip throughout the model. There are 79 out of the 2,500 ruptures that have dissimilarity values below the threshold, which is greater than any of the rupture classes for Japan or Chile. So, even though the Sumatra rupture is spatially larger and has relatively more dispersed slip throughout, stochastic modeling is still able to reproduce the rupture well.

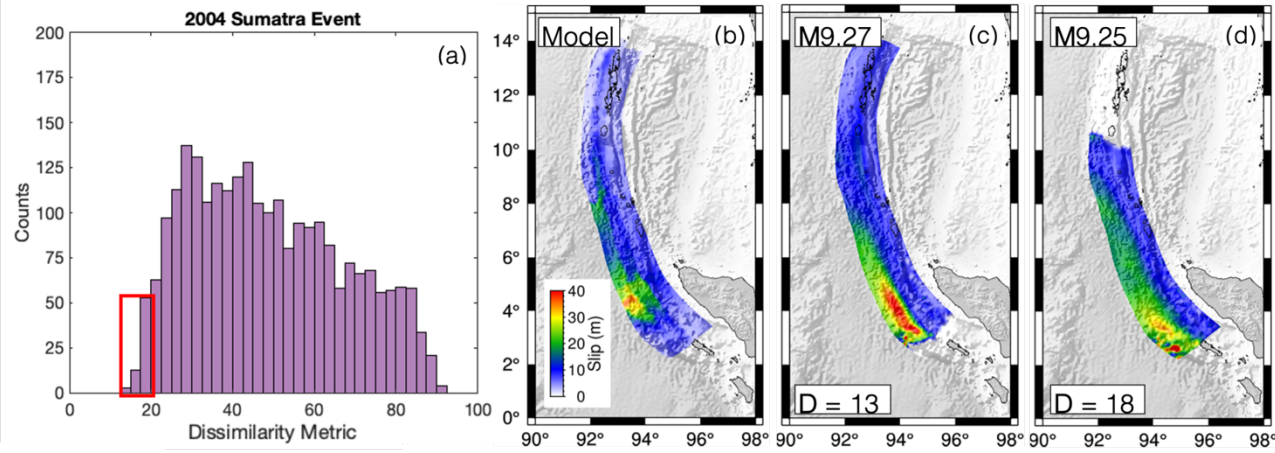

Figure 7: (a) Dissimilarity histogram distribution with a bin width of 2.5 for the 2004 Sumatra rupture. Red

4. Discussion

The three recorded earthquakes chosen for this study are all **M**9+ events that each are characterized by a unique coseismic slip distribution. The 2011 Tohoku rupture experienced near-trench slip over 70m, which had not been seen prior and was thought to be highly unlikely. The 1960 Chile event is the largest earthquake that has occurred during instrumental times, with three large slip asperities throughout the rupture area. Lastly, the 2004 Sumatra event ruptured a portion of the Sumatra-Andaman subduction zone over 1,300km long, a length that had never been observed before. The stochastic modeling approach can, at least to first order, reproduce realistic ruptures for all the three events we observed, without using coupling as an a priori constraint. With this in consideration, the stochastic slip modeling approach does have the capability

to represent large magnitude ruptures and therefore can be considered a viable option for certain rupture modeling applications such as probabilistic hazard analyses.

Small & Melgar (2021) argued that including coupling as a way to inform slip in the stochastic workflow has the potential to impact the technique's ability to create realistic ruptures. The analyses shown here argue that this can be true. The trench-locking class of Tohoku ruptures produces a greater percentage of ruptures below the dissimilarity threshold and generally leads to a tsunami inundation pattern that more closely replicates what was seen in the post-event survey. Compared to the homogeneous class, the trench-locking class has a probability of creating a "Tohoku-like" rupture that is 4 times more likely (57 total ruptures compared to 14 in the homogeneous class). Meanwhile for the trench-creeping class, no ruptures below the desired threshold are produced. This can be interpreted as the trench-creeping class has less ability to produce realistic ruptures. While including the "correct" coupling model has generally positive effects, including the "wrong" model can have very negative effects as well. So, a key finding in this work is that unless coupling is known with some certainty, for example, because it was obtained by including offshore geodetic measurements, it is safer to assume a homogenous distribution.

The drastic difference in the results of the two coupling models highlights the fundamental difference between them and the key characteristic of the Minson model. The 2011 Tohoku-Oki rupture was uncharacteristic when it first occurred because of the presence of large slip (~60-80 m) in the shallowest portion of the megathrust (Lay et al., 2018) (Figure 1a). In this model, the large slip asperity occurs below 20km in depth, with slip occurring up to the trench. The presence of shallow slip here is directly in contrast to the fundamental assumption of the trench-creeping class. Another direct result of the trench-creeping pattern of coupling is apparent in the tsunami inundation results. At intermediate dissimilarity values (35-50), the trench-creeping class has more accurate inundation results than the other two classes at the same dissimilarity values (Figure 5). For dissimilarity values where the other classes have inundation percentages less than 80%, most of the trench-creeping ruptures are greater than 80% inundated. This discrepancy is due to the location of dominant slip for the trench-creeping class ruptures. The region of largest slip deficit rate (and coupling ratio) is present is directly offshore of the Miyagi Prefecture along the Sanriku Coast (38.2°N). Because of this, the megathrust in this region typically has the largest slip in the hypothetical ruptures. Although slip occurring here is at depths greater than 25km, its proximity to the coast with enough amplitude can still create devastating tsunamis. So, even though a given rupture for the trench-creeping class has a larger dissimilarity value, it may still produce tsunami amplitudes that are similar to those of the real rupture.

The trench-locking class, on the other hand, is defined by a coupling pattern that correlates well with the Minson model. The trench-locking class has SDR accumulating all along the Japan trench, with over 40mm/yr of slip accumula-

tion occurring in the same location as the dominant slip patch in the Minson model. Since there are high SDR rates that correlate with areas of high slip in the Minson model, these areas will have a greater probability of producing higher slip in the calculated rupture models. When we are modeling ruptures, if the correct rupture geometry and magnitude are picked from the scaling laws, the trench-locking class will have the highest probability of reproducing the ruptures.

By adding the right coupling model, we can more likely produce "Tohoku-like" or realistic ruptures. This can be very helpful for future hazard studies in that we may be able to better produce realistic ruptures by including a model for coupling. However, as we have seen, the impact of choosing one model over the other produces drastically different results. Determining which coupling model is a difficult problem as it will require extensive seafloor instrumentation (e.g., Yokota et al., 2016). Luckily, the homogeneous class which does not utilize the coupling pattern still produces realistic ruptures as seen by all three of the example global earthquakes we calculated dissimilarity for. Although this produced fewer ruptures under the dissimilarity threshold than the trench-coupling class, it still has the capability to reproduce the slip models. So, rather than potentially misrepresenting the pattern of coupling, it is best to utilize the homogeneous method for stochastic modeling unless there is more certainty in the pattern of coupling.

Conclusion:

We tested whether the slip distributions calculated using stochastic slip rupture modeling are "realistic" by attempting to reproduce slip distributions that match what is seen in **M**9+ events recorded in instrumental time. We first started with the 2011 **M**9.1 Tohoku-Oki earthquake and tsunami where we tested both a stochastic method with a homogeneous background mean model and a method where slip is informed by an additional interseismic coupling constraint. We quantified the dissimilarity of slip distribution between the modeled ruptures and a slip inversion for the event. In addition to the slip pattern, we modeled high resolution tsunami inundation for 330 ruptures and compared the results to an inundation survey along the eastern coastline of Japan. We found that both the homogeneous and trench-locking classes could reproduce the 2011 Tohoku-Oki slip distribution defined by the Minson model and could model tsunami inundation results matching the post-earthquake tsunami survey. The trench-creeping class, however, could not produce any ruptures that qualified as "Tohoku-like," highlighting the varying effect a coupling constraint holds on the stochastic methodology. Because of the variable influence that either coupling model has on the output ruptures, we note that without strong reason to favor one coupling model over another, coupling should be excluded from the stochastic slip process to not introduce inaccurate biases. We also showed that for other great earthquakes such as the 1960 **M**9.4-9.6 Chile and 2004 **M**9.1-9.3 Sumatra stochastic slip modeling has the capability to produce realistic ruptures. So, although the trench-locking class outperformed the ho-

mogeneous class for the Tohoku earthquake, all three earthquakes studied here were able to be reproduced using the homogeneous background slip method for stochastic slip modeling. So, the traditional method for stochastic modeling is a viable option for further use. To end, we note that by increasing seafloor GNSS instrumentation at subduction zones, we may remedy the uncertainty of the coupling patterns in the shallow most portions of subduction zones so we can utilize the coupling constraint more confidently in future studies.

Data Availability

All synthetic ruptures for the three rupture groups (Tohoku, Chile, and Sumatra) are available for download on zenodo (DOI 10.5281/zenodo.6348094).

Works cited

Ammon, C. J., Lay, T., Kanamori, H., & Cleveland, M. (2011). A rupture model of the 2011 off the Pacific coast of Tohoku Earthquake. *Earth, Planets and Space*, *63*(7), 693-696.

Barnhart, W. D., Murray, J. R., Briggs, R. W., Gomez, F., Miles, C. P., Svarc, J., ... & Stressler, B. J. (2016). Coseismic slip and early afterslip of the 2015 Illapel, Chile, earthquake: Implications for frictional heterogeneity and coastal uplift. *Journal of Geophysical Research: Solid Earth*, *121*(8), 6172-6191.

Blaser, L., Krüger, F., Ohrnberger, M., & Scherbaum, F. (2010). Scaling relations of earthquake source parameter estimates with special focus on subduction environment. *Bulletin of the Seismological Society of America*, *100*(6), 2914-2926.

Hayes, G. P., Moore, G. L., Portner, D. E., Hearne, M., Flamme, H., Furtney, M., & Smoczyk, G. M. (2018). Slab2, a comprehensive subduction zone geometry model. *Science*, *362*(6410), 58-61.

Comninou, M., & Dundurs, J. (1975). The angular dislocation in a half space. *Journal of Elasticity*, *5*(3), 203-216.

Frankel, A., Wirth, E., Marafi, N., Vidale, J., & Stephenson, W. (2018). Broadband Synthetic Seismograms for Magnitude 9 Earthquakes on the Cascadia Megathrust Based on 3D Simulations and Stochastic Synthetics, Part 1: Methodology and Overall ResultsMethodology and Overall Results. Bulletin of the Seismological Society of America, 108(5A), 2347-2369.

Geuzaine, C., & Remacle, J. F. (2009). Gmsh: A 3-D finite element mesh generator with built-in pre-and post-processing facilities. International journal for numerical methods in engineering, 79(11), 1309-1331.

Goda, K., Yasuda, T., Mori, N., & Maruyama, T. (2016). New scaling relationships of earthquake source parameters for stochastic tsunami simulation. *Coastal Engineering Journal*, *58*(3), 1650010-1.

Grezio, A., Babeyko, A., Baptista, M. A., Behrens, J., Costa, A., Davies, G., ... & Thio, H. K. (2017). Probabilistic tsunami hazard analysis: multiple sources

and global applications. Reviews of Geophysics, 55(4), 1158-1198.

Ho, T. C., Satake, K., Watada, S., & Fujii, Y. (2019). Source estimate for the 1960 Chile earthquake from joint inversion of geodetic and transoceanic tsunami data. *Journal of Geophysical Research: Solid Earth*, *124*(3), 2812-2828.

Konca, A. O., Avouac, J. P., Sladen, A., Meltzner, A. J., Sieh, K., Fang, P., ... & Helmberger, D. V. (2008). Partial rupture of a locked patch of the Sumatra megathrust during the 2007 earthquake sequence. *Nature*, *456*(7222), 631-635.

Kragh, E. D., & Christie, P. (2002). Seismic repeatability, normalized rms, and predictability. *The leading edge*, *21*(7), 640-647.

Lay, T. (2018). A review of the rupture characteristics of the 2011 Tohoku-oki Mw 9.1 earthquake. *Tectonophysics*, *733*, 4-36.

LeVeque, R. J., George, D. L., & Berger, M. J. (2011). Tsunami modelling with adaptively refined finite volume methods. *Acta Numerica*, *20*, 211-289.

LeVeque, R. J., Waagan, K., González, F. I., Rim, D., & Lin, G. (2016). Generating random earthquake events for probabilistic tsunami hazard assessment. In *Global Tsunami Science: Past and Future, Volume I* (pp. 3671-3692). Birkhäuser, Cham.

Li, L., Switzer, A. D., Chan, C. H., Wang, Y., Weiss, R., & Qiu, Q. (2016). How heterogeneous coseismic slip affects regional probabilistic tsunami hazard assessment: A case study in the South China Sea. Journal of Geophysical Research: Solid Earth, 121(8), 6250-6272.

Li, S., & Freymueller, J. T. (2018). Spatial variation of slip behavior beneath the Alaska Peninsula along Alaska-Aleutian subduction zone. *Geophysical Research Letters*, *45*(8), 3453-3460.

Lin, J. T., Melgar, D., Thomas, A. M., & Searcy, J. (2021). Early warning for great earthquakes from characterization of crustal deformation patterns with deep learning. *Journal of Geophysical Research: Solid Earth*, *126*(10), e2021JB022703.

Lindsey, E. O., Mallick, R., Hubbard, J. A., Bradley, K. E., Almeida, R. V., Moore, J. D., ... & Hill, E. M. (2021). Slip rate deficit and earthquake potential on shallow megathrusts. *Nature Geoscience*, *14*(5), 321-326.

Loveless, J. P., & Meade, B. J. (2015). Kinematic barrier constraints on the magnitudes of additional great earthquakes off the east coast of Japan. *Seismological Research Letters*, *86*(1), 202-209.

Loveless, J. P., & Meade, B. J. (2016). Two decades of spatiotemporal variations in subduction zone coupling offshore Japan. *Earth and Planetary Science Letters*, *436*, 19-30.

Mai, P. M., & Beroza, G. C. (2002). A spatial random field model to characterize complexity in earthquake slip. *Journal of Geophysical Research: Solid Earth*,

107(B11), ESE-10.

Meade, B. J., & Loveless, J. P. (2009). Block modeling with connected fault-network geometries and a linear elastic coupling estimator in spherical coordinates. *Bulletin of the Seismological Society of America*, *99*(6), 3124-3139.

Melgar, D., & Bock, Y. (2015). Kinematic earthquake source inversion and tsunami runup prediction with regional geophysical data. *Journal of Geophysical Research: Solid Earth*, *120*(5), 3324-3349.

Melgar, D., & Hayes, G. P. (2019). The Correlation Lengths and Hypocentral Positions of Great EarthquakesThe Correlation Lengths and Hypocentral Positions of Great Earthquakes. *Bulletin of the Seismological Society of America*, *109*(6), 2582-2593.

Melgar, D., LeVeque, R. J., Dreger, D. S., & Allen, R. M. (2016). Kinematic rupture scenarios and synthetic displacement data: An example application to the Cascadia subduction zone. *Journal of Geophysical Research: Solid Earth*, *121*(9), 6658-6674.

Métois, M., Vigny, C., & Socquet, A. (2016). Interseismic coupling, megathrust earthquakes and seismic swarms along the Chilean subduction zone (38–18 S). *Pure and Applied Geophysics*, *173*(5), 1431-1449.

Métois, M., Socquet, A., Vigny, C., Carrizo, D., Peyrat, S., Delorme, A., ... & Ortega, I. (2013). Revisiting the North Chile seismic gap segmentation using GPS-derived interseismic coupling. *Geophysical Journal International*, *194*(3), 1283-1294.

Minson, S. E., Simons, M., Beck, J. L., Ortega, F., Jiang, J., Owen, S. E., ... & Sladen, A. (2014). Bayesian inversion for finite fault earthquake source models–II: the 2011 great Tohoku-oki, Japan earthquake. *Geophysical Journal International*, *198*(2), 922-940.

Moreno, M., Rosenau, M., & Oncken, O. (2010). 2010 Maule earthquake slip correlates with pre-seismic locking of Andean subduction zone. *Nature*, *467*(7312), 198-202.

Mori, N., Takahashi, T., & 2011 Tohoku Earthquake Tsunami Joint Survey Group. (2012). Nationwide post event survey and analysis of the 2011 Tohoku earthquake tsunami. *Coastal Engineering Journal*, *54*(1), 1250001-1.

Oleskevich, D. A., Hyndman, R. D., & Wang, K. (1999). The updip and downdip limits to great subduction earthquakes: Thermal and structural models of Cascadia, south Alaska, SW Japan, and Chile. *Journal of Geophysical Research: Solid Earth*, *104*(B7), 14965-14991.

Okada, Y. (1985). Surface deformation due to shear and tensile faults in a half-space. *Bulletin of the seismological society of America*, *75*(4), 1135-1154.

Perfettini, H., Avouac, J. P., Tavera, H., Kositsky, A., Nocquet, J. M., Bondoux, F., ... & Soler, P. (2010). Seismic and aseismic slip on the Central Peru

megathrust. *Nature*, *465*(7294), 78-81.

Razafindrakoto, H. N., Mai, P. M., Genton, M. G., Zhang, L., & Thingbaijam, K. K. (2015). Quantifying variability in earthquake rupture models using multidimensional scaling: Application to the 2011 Tohoku earthquake. *Geophysical Journal International*, *202*(1), 17-40.

Rodriguez, E. E., & Russo, R. M. (2020). Southern Chile crustal structure from teleseismic receiver functions: Responses to ridge subduction and terrane assembly of Patagonia. *Geosphere*, *16*(1), 378-391.

Rhie, J., Dreger, D., Burgmann, R., & Romanowicz, B. (2007). Slip of the 2004 Sumatra–Andaman earthquake from joint inversion of long-period global seismic waveforms and GPS static offsets. *Bulletin of the Seismological Society of America*, *97*(1A), S115-S127.

Salazar-Monroy, E. F., Melgar, D., Jaimes, M. A., & Ramirez-Guzman, L. (2021). Regional Probabilistic Tsunami Hazard Analysis for the Mexican Subduction Zone from Stochastic Slip Models. Journal of Geophysical Research: Solid Earth, 126(6), e2020JB020781.

Satake, K., Fujii, Y., Harada, T., & Namegaya, Y. (2013). Time and space distribution of coseismic slip of the 2011 Tohoku earthquake as inferred from tsunami waveform data. *Bulletin of the seismological society of America*, *103*(2B), 1473-1492.

Small, D. T., & Melgar, D. (2021). Geodetic coupling models as constraints on stochastic earthquake ruptures: An example application to PTHA in Cascadia. *Journal of Geophysical Research: Solid Earth*, *126*(7), e2020JB021149.

Tozer, B., Sandwell, D. T., Smith, W. H., Olson, C., Beale, J. R., & Wessel, P. (2019). Global bathymetry and topography at 15 arc sec: SRTM15+. *Earth and Space Science*, *6*(10), 1847-1864.

Villegas-Lanza, J. C., Chlieh, M., Cavalié, O., Tavera, H., Baby, P., Chire-Chira, J., & Nocquet, J. M. (2016). Active tectonics of Peru: Heterogeneous interseismic coupling along the Nazca megathrust, rigid motion of the Peruvian Sliver, and Subandean shortening accommodation. Journal of Geophysical Research: Solid Earth, 121(10), 7371-7394.

Wang, K., & Tréhu, A. M. (2016). Invited review paper: Some outstanding issues in the study of great megathrust earthquakes—The Cascadia example. *Journal of Geodynamics*, *98*, 1-18.

Williamson, A., Melgar, D., & Rim, D. (2019). The effect of earthquake kinematics on tsunami propagation. *Journal of Geophysical Research: Solid Earth*, *124*(11), 11639-11650.

Wilson, D. L., Baddeley, A. J., & Owens, R. A. (1997). A new metric for grey-scale image comparison. *International Journal of Computer Vision*, *24*(1), 5-17.

Yokota, Y., Ishikawa, T., Watanabe, S. I., Tashiro, T., & Asada, A. (2016). Seafloor geodetic constraints on interplate coupling of the Nankai Trough megathrust zone. Nature, 534(7607), 374-377.

Yue, H., & Lay, T. (2011). Inversion of high-rate (1 sps) GPS data for rupture process of the 11 March 2011 Tohoku earthquake (Mw 9.1). *Geophysical Research Letters*, *38*(7).